
Wave spectrum retrieval from airborne sunglitter images

Yurovskaya Maria^{1,2,*}, Rasclé Nicolas^{3,4}, Kudryavtsev Vladimir^{1,2}, Chapron Bertrand^{2,4}, Marie Louis⁴, Molemaker Jeroen⁴

¹ RAS, Marine Hydrophys Inst, Sevastopol, Russia.

² Russian State Hydrometeorol Univ, Satellite Oceanog Lab, St Petersburg, Russia.

³ Ctr Invest Cient & Educ Super Ensenada, Div Oceanol, Ensenada, Baja California, Mexico.

⁴ Inst Francais Rech Exploitat Mer, Plouzane, France.

* Corresponding author : Maria Yurovskaya, email address : mvkosnik@gmail.com

Abstract :

Reconstruction and evolution of two-dimensional spectra of surface waves in the Gulf of Mexico are derived from airborne sun-glitter imagery. As the proposed method is based on a linear transfer function deduced from the shape of the sunglitter brightness, the absolute wavenumber elevation spectrum does not require any additional assumption or information about sky brightness, wind or wave energy. The detailed description of the airborne image processing method is given. As demonstrated, retrieved spectra agree well with nearby NDBC buoy data, both for spectrum shape, level and energy angular distribution. The 180-degree wave direction ambiguity, inherent to image-derived spectra, is eliminated by using cross-correlation analysis between two consecutive images. A case study corresponding to the spectral evolution with increasing distance from shore in slanting fetch conditions is then considered. Energy level and peak position transformation are consistent with established approximations and laws of wind-sea development. The technical requirements (flight altitude, image resolution, view angles, etc) and applicability of the suggested methodology are also discussed. These results demonstrate the potential efficiency of high resolution sea state monitoring from drones or light aircrafts using sunglitter imagery.

Highlights

► Sea surface wave spectra are derived from airborne sunglitter imagery. ► A linear transfer function relates sunglitter brightness and wave elevation spectra. ► The method is applied to airborne images taken in the Gulf of Mexico. ► A case study on the spectral evolution with fetch increasing is considered. ► The technical requirements and method applicability are discussed.

Keywords : Sunglitter, Sea surface waves, Directional wave spectrum, Aerial photography, Field measurements, Remote sensing observations, High resolution, Drone

16 **1. Introduction**

17 For a wide range of applications, such as coastal management, the design
18 and operational safety of harbours, ships, and offshore structures, a precise
19 knowledge of the directional spectrum of ocean waves is needed. The di-
20 rectional wave spectrum describes the distributed energy contributions from
21 waves propagating in different directions with different wavelengths. It is key
22 to help determine the consequences of interactions between waves and other
23 structures, i.e. breakwaters and offshore structures, but also to evaluate

24 wave-induced upper ocean transport and erosion processes.

25 Significant advances have thus been made to estimate these directional
26 wave statistical properties. Today, a large number of measuring devices,
27 working on different principles, are available (e.g. Herbers et al., 2012). Yet,
28 the directional and frequency response of these systems may often be limited
29 and not sufficient to fully resolve directional surface wave spectra. Further,
30 requirements for near-simultaneous, high spatial resolution observations, to
31 provide more direct directional wavenumber measurements of the local sur-
32 face field over entire regions, has attracted the attention on remote sensing
33 technologies. To complement sparse in-situ buoy measurements, techniques
34 can include sea level radars (coastal HF radars, Barrick and Lipa, 1985),
35 microwave and marine X-band radars (Senet et al., 2008; Nieto et al., 2004),
36 scanning altimeter and lidar high-resolution topography instruments from
37 airplane platforms (Walsh et al., 1998; Melville et al., 2016), and also syn-
38 thetic aperture or rotating real-aperture airborne radar instruments (Caudal
39 et al., 2014). As well, photographs of the ocean surface have long been
40 proved to contain quantitative information about ocean surface slope statis-
41 tics (e.g. Barber, 1949; Cox and Munk, 1956), to help infer directional spectra
42 of surface waves (Stilwell, 1969; Stilwell and Pilon, 1974). Today, with the

43 significant cost reduction and improvement of both instruments and drones,
44 the photograph techniques may become more widely used to observe and
45 monitor surface waves at regional or coastal scales.

46 Since almost two centuries (Spooner, 1822), it has been understood that
47 the shape of the sunglint on the sea surface contains information on the
48 statistical properties of wave slopes. Airborne and satellite sunglint images
49 at medium (~ 1 km) resolution have then been used to precisely estimate
50 sea surface slope statistical properties (Cox and Munk, 1956; Breon and
51 Henriot, 2006), and modulations by various dynamical ocean processes like
52 currents and fronts, internal waves, or surface slicks (Barber, 1954; Apel
53 et al., 1975; Hennings et al., 1994; Kudryavtsev et al., 2012; Kudryavtsev
54 et al., 2012; Rasche et al., 2016, 2017). At higher ($\sim 1 - 10$ m) resolution,
55 glitter modulations are more directly connected to the wavy surface. Indeed,
56 wave contrasts on the image result from the modulation of sun reflected
57 radiation by individual tilting wave slopes, and those can be used to estimate
58 the wave directional elevation spectrum (Stilwell and Pilon, 1974; Monaldo
59 and Kasevich, 1981).

60 To derive wave elevations from these brightness variations, a transfer func-
61 tion must thus be determined. Using airborne photographs, this task is eased,

62 as the overall sunglitter shape can be captured, to help directly infer a linear
63 transfer function (Bolshakov et al., 1988). Recently, Yurovskaya et al. (2018)
64 demonstrated the technical implementation to retrieve wind wave spectrum
65 from sunglitter photographs taken from a drone. Adapted to a satellite con-
66 figuration, such a method was also successfully applied (Kudryavtsev et al.,
67 2017a,b) to reconstruct the spectrum of long (energy containing) waves from
68 satellite sunglitter images, taking advantage of the high resolution and spe-
69 cific viewing geometry of the radiometers on-board the satellite Sentinel-2.

70 In this paper, we further dwell on this capability of airborne sunglitter
71 imagery to capture the overall glitter pattern. As mentioned above, this
72 property provides direct means to determine a linear transfer function. Our
73 motivation is then to further assess how robust is our proposed methodology
74 to efficiently provide quantitative estimates of the directional wave spectrum,
75 including energy containing waves and also short waves. The development
76 is specific to airborne measurements and applied to data collected over a
77 coastal area in the northern Gulf of Mexico.

78 The paper structure is as follows. The experiment is described in Sec-
79 tion 2; theory and spectrum reconstruction algorithm are presented in Sec-
80 tion 3; method implementation and validation are given in Section 4; the

81 results of the study of wave development and transformation with fetch are
82 presented in Section 5, and finally, the discussion of method applicability and
83 some recommendations on experimental setup are suggested in Section 6.

84 **2. Experiment and Data**

85 The airborne sunglitter images were obtained on Jan. and Feb. 2016
86 during the Lagrangian Submesoscale Experiment (LASER), where a large
87 number (~ 1000) of surface drifters were deployed to study surface dispersion
88 within the Gulf of Mexico (D’Asaro et al., 2018; Rasche et al., 2017), close to
89 the site of the Deep Horizon oil platform accident in 2010 (Fig. 1, a). The
90 images were acquired from airplane (a Partenavia P.68) flying at altitudes
91 up to 3000 m.

92 The visible light intensity was measured by two panchromatic cameras
93 (JAI BM-500GE) equipped with a 5 mm focal length low distortion lens to
94 ensure a large field of view. The cameras setup is sketched in Figure 1, b. To
95 capture the sunglint, the two cameras were arranged symmetrically about
96 the airplane nadir with a pitch of $\pm 35^\circ$ for the forward/aftward cameras.
97 The camera aperture angles are $80^\circ \times 70^\circ$ along-track and across-track, re-
98 spectively, with 2456×2058 pixels in the respective directions. For a flight

99 altitude of 1000 m, this leads to a ground resolution from 0.5 m to 6 m. The
100 cameras acquired images at 2 Hz. The images were geolocated using an in-
101 ternal motion unit Applanix POS AV V610.

102 We selected cases corresponding to measurements made during flights
103 with trajectories close to National Data Buoy Center (NDBC) buoy locations,
104 to benefit from synchronous wind and wave ancillary data. A step by step
105 algorithm is provided for images obtained close to NDBC 42012 in developed
106 wind sea conditions on 11-Feb-2016 (green star on Fig. 1, a). Further we
107 analyze the wave evolution on 23-Jan-2016, when sunglitter images were
108 acquired (in cloudless regions) at different distances from the shore along the
109 plane tracks shown in Fig. 1, a.

110 **3. Theoretical Background**

111 Based on the classical model of the sea surface brightness formation in the
112 visible range (Cox and Munk, 1956), the intensity in each pixel of sunglitter
113 image is proportional to the sun reflected radiance, or the energy brightness
114 of the surface (the spectral energy flux per unit area per unit solid angle):

$$N = \frac{\rho E_s}{4 \cos \theta \cos^4 \beta} P(Z_1, Z_2), \quad (1)$$

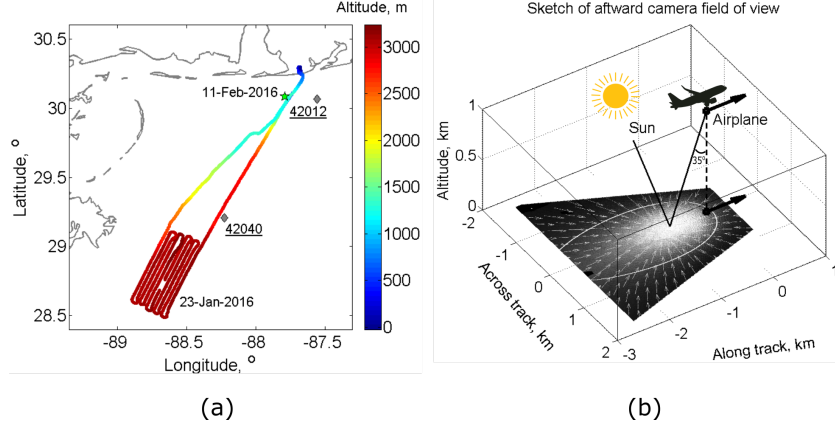


Figure 1: (a) The observation area with NDBC buoy locations (gray diamonds). Green star shows location of the analysis on 11-Feb-2016 (section 4), colors are the tracks of the 23-Jan-2016 flight (section 5). (b) Sketch of the field of view of the afterword camera, for a flight altitude of 1000 m. Here we show the special case of the sun exactly at the rear of the airplane when the specular sun spot is at the center of the camera field of view. The ellipse is the contour $Z_n^2 = s^2$ (see the notifications below). The white arrows show the orientations of the transfer function gradient, G_{zi} .

115 where P is the probability density of two slope components, Z_1, Z_2 , satisfying

116 the conditions of specular reflection:

$$\begin{aligned}
 Z_1 &= -\frac{\sin \theta_s \cos \phi_s + \sin \theta \cos \phi_\nu}{\cos \theta_s + \cos \theta} \\
 Z_2 &= -\frac{\sin \theta_s \sin \phi_s + \sin \theta \sin \phi_\nu}{\cos \theta_s + \cos \theta},
 \end{aligned} \tag{2}$$

117 θ and θ_s are zenith angles for the camera and the sun, respectively, ϕ_ν and

118 ϕ_s are corresponding azimuth angles, ρ is the Fresnel reflection coefficient,

119 E_s is the solar radiance, $\tan \beta = \sqrt{Z_1^2 + Z_2^2}$.

120 Local modulations of $B = N \cos \theta / \rho$, or equivalently, of P , can arise for
121 two reasons: variations of the slope statistics mostly governed by changes
122 of mean square slope (MSS) due to different upper ocean processes (fronts,
123 internal waves, surface slicks, etc), or the tilting of the ocean surface while a
124 long wave is propagating. The latter can also lead to a short wave (and thus,
125 MSS) modulation along the wave profile. As demonstrated by Bolshakov
126 et al. (1988) and Kudryavtsev et al. (2017a), one can ignore these MSS
127 modulations in the vicinity of brightness contrast inversion zone, i.e. $0.5 <$
128 $Z_n^2/s^2 < 2$, where $Z_n^2 = Z_1^2 + Z_2^2$, and s^2 is the surface MSS to the first order
129 estimated from the assumption of Gaussian brightness and slope distribution
130 as $s^2 = -2\overline{Z_n} \cdot \overline{B}/(\partial B/\partial Z_n)$. The brightness variation due to the long wave
131 propagation then writes:

$$\tilde{B} = B(Z_1 + \zeta_1, Z_2 + \zeta_2) - B(Z_1, Z_2) = \frac{\partial B}{\partial Z_i} \zeta_i \equiv G_{zi} \zeta_i, \quad (3)$$

132 where $\zeta_{1,2}$ are the components of tilting wave slope. G_{zi} is the transfer
133 function, relating brightness and slope variations. This transfer function is
134 then determined as the brightness gradient in specular slope space and can
135 be obtained through the observed brightness gradients:

$$\begin{aligned}
G_{z1} &= (G_2 Z_{2,1} - G_1 Z_{2,2})/\Delta \\
G_{z2} &= (G_1 Z_{1,2} - G_2 Z_{1,1})/\Delta,
\end{aligned}
\tag{4}$$

136 where $G_i = \partial B/\partial x_i$, $Z_{i,j} = \partial Z_i/\partial x_j$, $\Delta = Z_{1,2}Z_{2,1} - Z_{1,1}Z_{2,2}$.

137 Eq. (1) relates the mean brightness to surface slope statistics, as in the
138 work of Cox and Munk (1954). On the contrary, (3) and (4) relate local
139 brightness variations to local slope variations. In the Fourier space the surface
140 slope ζ_j and the surface elevation ξ are linked by: $\hat{\zeta}_j = ik_j \hat{\xi}$, where i stands for
141 imaginary unit. Thus, equation (3) in the Fourier space reads: $\hat{B} = ik_j G_{zj} \hat{\xi}$,
142 and the relationship between the surface elevations and brightness spectra
143 writes:

$$S_\xi(\mathbf{k}) = S_B(\mathbf{k})/(G_{zi}k_i)^2.
\tag{5}$$

144 The linear combination of wave vector components in the denominator
145 of (5) vanishes in a direction perpendicular to the gradient direction. Close
146 to this direction, the spectrum cannot be simply retrieved. For Sentinel-
147 2 multi-spectral satellite imagery, recently reported by Kudryavtsev et al.

148 (2017a,b), this limitation was mitigated by interpolating the spectrum in a
 149 narrow wavenumber sector encompassing the singularity. A clear advantage
 150 of airborne photography (compared with satellite scanners) is that it cap-
 151 tures the two-dimensional field of view of the sunglitter brightness. Therefore,
 152 relation like (5) can be obtained in different parts of the sunglitter, corre-
 153 sponding to directions for which the brightness gradients are different. As
 154 suggested by Bolshakov et al. (1988) and also Lupyan (1988), the singularity
 155 can be eliminated, by using several image fragments with different gradients
 156 G_{zi}^n , but statistically identical wave spectrum, $S_{\xi}^n(\mathbf{k}) = S_{\xi}(\mathbf{k})$. As sketched
 157 in Fig. 1, b, where the typical distribution of G_{zi}^n orientations is shown, the
 158 vectors converge towards the sunglitter center, changing their direction from
 159 0° to 360° around it. Brightness spectra taken from fragments with different
 160 vector orientations can then be averaged, to obtain the elevation spectrum
 161 without any singularity:

$$S_{\xi}(\mathbf{k}) = \sum_{n=1}^N S_B^n(\mathbf{k}) / \sum_{n=1}^N (G_{zi}^n k_i)^2. \quad (6)$$

162 As described, the considered methodology is self-consistent, solely based
 163 on the transfer function estimation from the observed shape of solar glint.
 164 For airborne photography, the following steps must then be taken:

- 165 • gradients G_i , $Z_{i,j}$ are determined from the smoothed sunglitter pattern
166 and known geometrical parameters;
- 167 • a transfer function, G_{zi} , is calculated using (4);
- 168 • several image fragments are selected in different image parts, still in
169 the vicinity of contrast inversion zone, and their brightness spectra are
170 calculated;
- 171 • the absolute directional wave elevation spectrum is derived from the
172 sum of brightness spectra and transfer function field, using expression
173 (6);
- 174 • 180-degree wave direction ambiguity can be removed using cross-correlation
175 analysis of two consequent images.

176 A detailed example of airborne sunglitter image processing is given below.

177 4. Method Implementation

178 4.1. Image preprocessing

179 On 11-Feb-2016, a snapshot of the sea surface (Fig. 2, a) was extracted
180 close to the location of the NDBC buoy number 42012 (Fig. 1, a). The wind

181 was about 9 m s^{-1} blowing from South-West, and peak waves of about 40 m
182 wavelength were propagating from the same direction.

183 The above procedure must be applied to a brightness field predominantly
184 formed by the sunlight reflections from the sea surface. Besides the image
185 projection onto the sea surface plane (Fig. 2, b), a preparatory step is to
186 consider an intensity correction to possibly account for extraneous factors
187 hampering the image brightness. We neglect any vignetting effect and con-
188 sider the image intensity proportional to the energy surface brightness, N .
189 First, the sky reflection and scattered radiation can contribute to the image
190 brightness. Cox and Munk (1956) report corresponding dependencies on in-
191 cidence angle by considering intensities from regions far outside the glitter.
192 A similar procedure is to use the darkest column of the photograph (the right
193 one in the example on Fig. 2, a). Given the viewing geometry and neglect-
194 ing the sunlitter contribution within this darkest line, the incidence angle
195 dependency of the background radiance can be estimated. A correspond-
196 ing polynomial approximation, Fig. 2, c, is then assumed to extend over the
197 whole 2D image, and further subtracted. Nevertheless, in all considered ex-
198 amples, we do not use parts of the images with $\theta > 50^\circ$, areas over which the
199 impact of scattered radiation rapidly grows (Cox and Munk, 1956), and the

200 assumption (3) loses its validity.

201 According to (1), the detrended field, $N - N_{back}$ (not shown), should
202 be multiplied by $\cos\theta/\rho$, shown in Fig. 2, d. Values of $\cos\theta/\rho$ differ up
203 to 4-5 times on the opposite image borders with incidence angles 25° and
204 60° . This operation suppresses the brightness of the distant zone and shifts
205 the sunglitter center towards the edge corresponding to the lowest incidence
206 angle (compare Fig. 2, b and Fig. 2, e). The mean brightness field, B_0
207 (Fig. 2, f), is then derived by smoothing $B = (N - N_{back}) \cos\theta/\rho$ using a
208 moving average filter, with a window size depending on the image resolution
209 (about several lengths of dominant wave). All the algorithm steps then apply
210 to the brightness variation field, $B - B_0$.

211 4.2. Spectrum validation

212 A fragment of the brightness variation field is shown Fig. 3, a. Fragments
213 are taken between the two ellipses indicating the zone $0.5 < Z_n^2/s^2 < 2$, and
214 above the line $\theta = 50^\circ$.

215 Fig. 3, b displays the sum of directional brightness spectra. As expected,
216 the resulting transfer function, $\sum(G_{zi}^n k_i)^2$ (Fig. 3, c), does not vanish in
217 any particular direction, but tends to zero in the wavenumber plane center.
218 This may enhance noise level and errors at the lowest wavenumbers. After

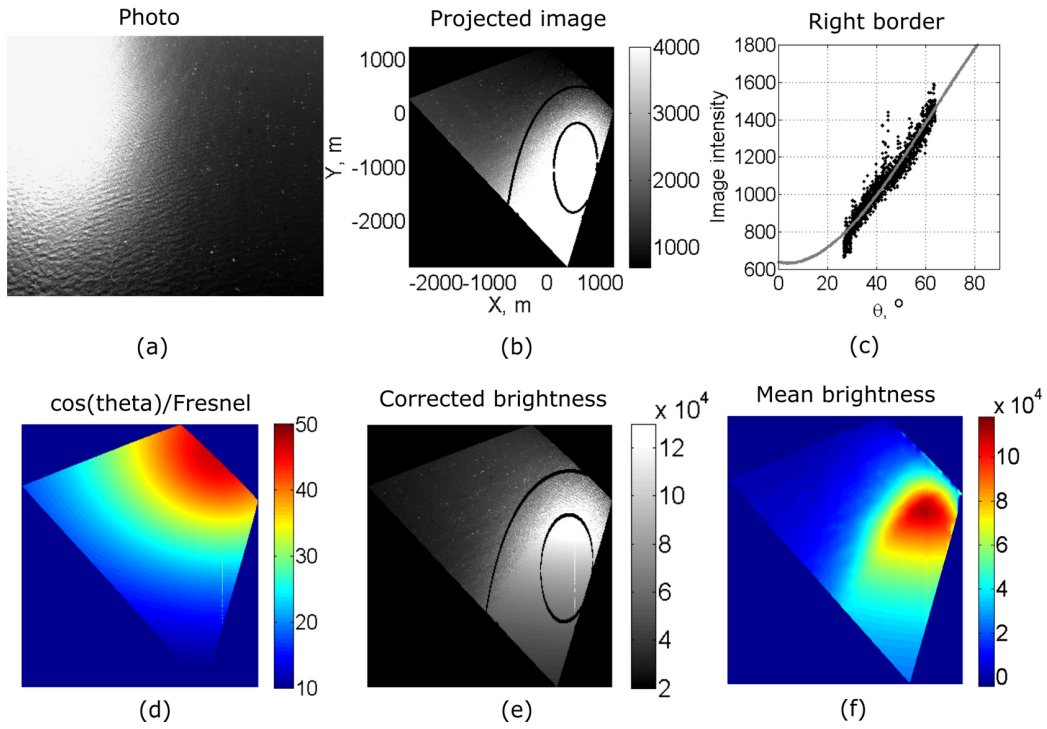


Figure 2: (a) An airborne snapshot of a sea surface; (b) image projected on the sea surface plane (x-label is to the East, y-label is to the North, two ellipses determine the zone $0.5 < Z_n^2/s^2 < 2$); (c) pixel intensities for the left column of a photo (dots) and their polynomial approximation indicating the background radiation; (d) $\cos \theta/\rho$ field; (e) $B = (N - N_{back}) \cos \theta/\rho$ field; (f) mean brightness field, B_0

219 application of the transfer function, Fig. 3, d, both brightness and wave
220 elevation spectra possess a distinct spectral peak, visually corresponding to
221 the waves observed on the fragment, Fig. 3, a, but the angular distribution
222 of the elevation spectrum is apparently broader, possibly revealing waves
223 moving closer to zonal (eastward or westward) directions.

224 The comparison with the nearby NDBC buoy wavenumber directional
225 spectrum (Fig. 3, d), calculated with the use of the maximum entropy method
226 (Lygre and Krogstad, 1986) and linear dispersion relation for gravity waves,
227 gives a satisfactory agreement of 2D energy distribution. Notice that in
228 contrast to NDBC data that provides a “true” directional spectrum, the
229 spectrum retrieved from the image is folded ($S(\phi) = S(\phi) + S(\phi + 180^\circ)$)
230 having a 180-degree ambiguity in wave direction.

231 Omnidirectional spectra are compared in Fig. 3, f, and give an excellent
232 agreement of peak position and its energy level. Energy underestimation
233 of retrieved spectrum at wavenumbers $k > 0.3$ rad/m can be explained by
234 the actual (not interpolated) image resolution and smoothing of features
235 smaller than 10 m. The noise level at $k < 0.1$ rad/m depends on the B_0
236 calculation (the smaller the filter window size, the lower the spectrum), and
237 is also controlled by the singularity of a transfer function around $k = 0$ rad/m.

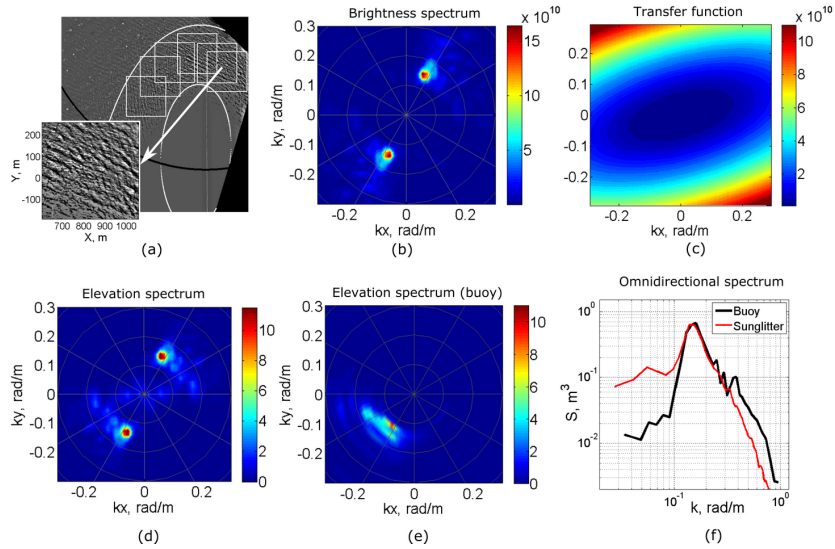


Figure 3: (a) Square fragments (450 m size) of brightness variation field, $(B - B_0)$, taken for spectrum retrieval. Two ellipses determine the zone $0.5 < Z_n^2/s^2 < 2$, black line is $\theta = 50^\circ$; (b) The sum of brightness spectra; (c) the transfer function, $\sum_{n=1}^N (G_{zi}^n k_i)^2$; (d) retrieved from (6) elevation spectrum; (e) NDBC buoy data directional spectrum (42012); (f) Omnidirectional spectra comparison.

238 Energy distribution of waves in a range 20 m - 60 m is reliably reproduced.

239 4.3. Wave direction ambiguity

240 In our cases, the camera acquired images every 0.5 s. Consecutive snap-
 241 shots can then be analyzed to remove the wave propagation directional
 242 ambiguity (Fig. 3, d), as already demonstrated for satellite measurements
 243 (Kudryavtsev et al., 2017a; De Michele et al., 2012). Two images of the
 244 same square region of the sea surface taken with a $\Delta t = 0.5$ s time difference
 245 are shown on Fig. 4, a-b. Their spectral coherence, $\langle \hat{I}_2 \hat{I}_1^* \rangle^2 / (\langle \hat{I}_1 \hat{I}_1^* \rangle \langle \hat{I}_2 \hat{I}_2^* \rangle)$

246 $\hat{I}_2 \hat{I}_2^*$ \rangle), hat means the Fourier transform, a star is complex conjugation,
 247 and phase, $\arg(\langle \hat{I}_2 \hat{I}_1^* \rangle)$, are given in Fig. 4, b-c. The coherence level is
 248 high, up to 1, in the direction where the waves are observed. The phase
 249 spectrum is a-priori asymmetric, and the positive phase shift corresponds to
 250 the direction “from” in a case when I_1 is taken earlier than I_2 . Thus, the
 251 wave system is moving from South-West, to agree with the NDBC directional
 252 spectrum (Fig. 3, b).

253 Airborne image time series can further be used to estimate ocean surface
 254 currents from the dispersion of the detected gravity waves (e.g. Dugan and
 255 Piotrowski (2003)). Taking a transect in the phase spectrum, $\Delta\Phi$, along a
 256 direction corresponding to maximum coherency, marked with a dashed line
 257 in Fig. 4, the dispersion can be evaluated for the relative projection of the
 258 phase velocity: $c(k) = \frac{\Delta\Phi/\Delta t}{k}$. As obtained, Fig. 4, e, experimentally derived
 259 points lie very close to the standard prediction, $c = \sqrt{g/k}$, even at large
 260 wavenumbers for which the elevation spectral analysis is less reliable. This
 261 indicates the absence of surface current, or at least its component along the
 262 chosen direction, in the region of observation.

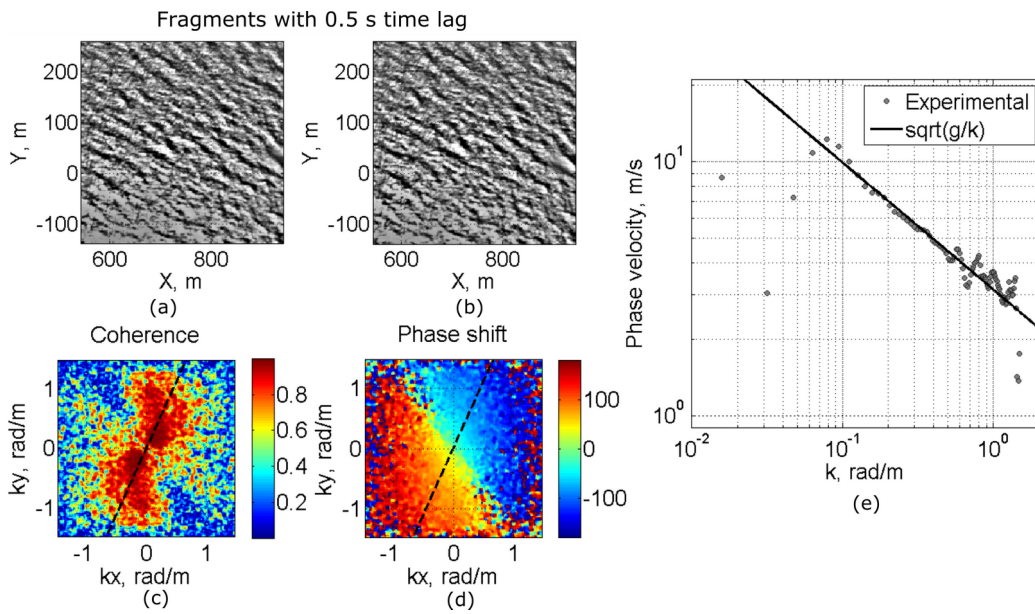


Figure 4: (a)-(b) Snapshots of the same location taken with 0.5 s time shift; (c) coherence of two brightness fields; (d) phase shift; wave direction (from) corresponds to positive values of a phase shift; (e) dispersion relation calculated from a phase shift along the line of coherence maximum (dashed lines in (c) and (d) plots).

263 5. A Case Study: Spectrum Evolution with Fetch

264 On 23-Jan-2016, an experiment to study wave transformation at varying
265 distance from the shore was conducted. The airplane moves seawards across
266 the NDBC 42012 and 42040 locations (Fig. 1, a, and Fig. 5). The flight
267 started at 19:20 UTC in clear sky conditions, but at 19:31 the plane entered
268 a cloudy zone with gleam areas too small to estimate the wave spectrum. Yet,
269 two images at 19:50 could be exploited. On the way back, at 23:00, camera
270 pitch and sun elevation angle didn't satisfy the condition $Z_n^2/s^2 < 2$ and
271 clouds were still hindering the glitter. As a result, only one image fragment
272 from the glint periphery could be used, with relatively low reliability.

273 The wind speed and direction (in nautical system) around the time of
274 acquisition are plotted in Fig. 6. Wind was blowing from the North-West,
275 slightly rotating clockwise and calming down from 12 m s^{-1} to 10 m s^{-1} ,
276 accordingly to NDBC 42040 data. The slow clockwise wind rotation took
277 place during the previous two days, starting to blow from South, then West,
278 before finally subsiding to 3 m s^{-1} from North on 24-Jan.

279 The two-dimensional slope spectra (Sk^2) from the buoys are shown in
280 Fig. 6. The slope spectra, reconstructed from the airplane images are shown
281 in Fig. 7, for the points marked by red squares on the map of Fig. 5. Many

282 different wave systems co-exist in the area (see sketch Fig. 5).

283 First, there is a long ($k \sim 0.05 \text{ rad m}^{-1}$) swell from West-South-West,
284 probably originating from West of the Mississippi delta and entering the area
285 from the South-West. This swell is well observed at buoy 42040 (Fig. 6,
286 bottom right) and on the airplane spectra at 22:50 (Fig. 7). It is not properly
287 resolved by the small image fragments used around buoy 42012 and is weakly
288 seen on the buoy data (Fig. 6, bottom left) as the Southern swell.

289 Also, there is the wind sea at short wavenumbers ($k > 0.1 \text{ rad m}^{-1}$). The
290 peak of the wind sea is slightly more from the North than the wind direction
291 (marked by a white dashed line in Fig. 6 and Fig. 7), both on buoy data and
292 on the airplane spectra. Third, there is a series of spectral peaks from West
293 to North-West (see before 19:31 on Fig. 7, see also buoy data on Fig. 6).
294 Those peaks are typical of slanting fetch conditions (Ardhuin et al., 2007,
295 e.g.), where the wind sea separates between subsystems, the high-frequency
296 remaining downwind whereas waves at relatively lower frequency develop
297 and propagate in the slanting fetch direction (along-shore). Very close to the
298 shore (before 19:25 on Fig. 7), those slanting short waves even dominate the
299 wind sea spectrum.

300 From the analyzed spectra, the main tendency is a gradual peak shift-

301 ing towards lower wavenumbers and a corresponding energy growth with the
302 fetch distance. These effects are better identified in omnidirectional spectrum
303 evolution, Fig. 8. The figure presents angle-integrated surface elevation spec-
304 trum (red) together with buoy-derived spectra at 19:00 (t1, black) and 20:00
305 (t2, gray) for NDBC 42012, and at 21:00 (t1) and 23:00 (t2) for NDBC 42040.
306 To help the interpretation, empirical model spectra, as suggested by Donelan
307 et al. (1985) and Babanin and Soloviev (1998), are displayed, for different
308 fetches (given in figure titles). Fetches are calculated as the distance to the
309 line passing through alongshore islands (bold green on Fig. 5) in the direc-
310 tion of the wind taken from the nearest buoy. They are further corrected to
311 account for the direction of the spectral peak mostly deviating from NDBC
312 wind direction. At small fetches (below 5-10 km), the spectrum is rather
313 variable in energy level and peak position, also probably due to the changing
314 bottom topography and consequent refraction effects. The wind wave peak
315 is hardly distinguished and only starts to be clearly obtained at fetch about
316 10 km. At 19:25:31, the fetch value is close to the one captured at NDBC
317 42012 location (see Fig. 5). The respective spectra are then found very close
318 (compare black and red curves in Fig. 8). The evolution then continues and
319 closely follows Donelan et al. (1985) and Babanin and Soloviev (1998) pre-

320 ditions. Despite the low reliability for the sunglitter-derived spectrum at
321 22:50 (the last subplot), a good agreement is found with both model and
322 buoy data taken at approximately the same fetch.

323 To generalize the wind sea peak transformation, we present (Fig. 9, a)
324 the dependency of dimensionless peak frequency, $f_p u_{10}/g$, and dimensionless
325 energy, Eg^2/u_{10}^4 , estimated as the spectrum integral around the wind wave
326 peak and shorter waves, on dimensionless wave fetch, Lg/u_{10}^2 . Comparison is
327 made with other data collected by Babanin and Soloviev (1998). As obtained,
328 results are consistent with the cited approximations, except for the wave
329 energy at the near-shore points. For these cases, the wind peak wavelength
330 is not far from the camera resolution.

331 The present data, unfortunately, cannot trace any pronounced tendency
332 for the angular distribution evolution. This is due to the presence of sev-
333 eral swell peaks much stronger than the wind ones, and inaccurate data at
334 large fetches, where the wind peak dominates. Yet, the average angular
335 distribution around the peak wavenumber (Fig. 9, b) does not contradict
336 the dependency, $S(k_p) = 0.5\beta/\cosh^2(\beta\phi)$, $\beta = 2.28$, reported by Donelan
337 et al. (1985), confirming that multi-modal spectrum structure provides some
338 broadening at the angles far from $\phi = 0$ (peak position).

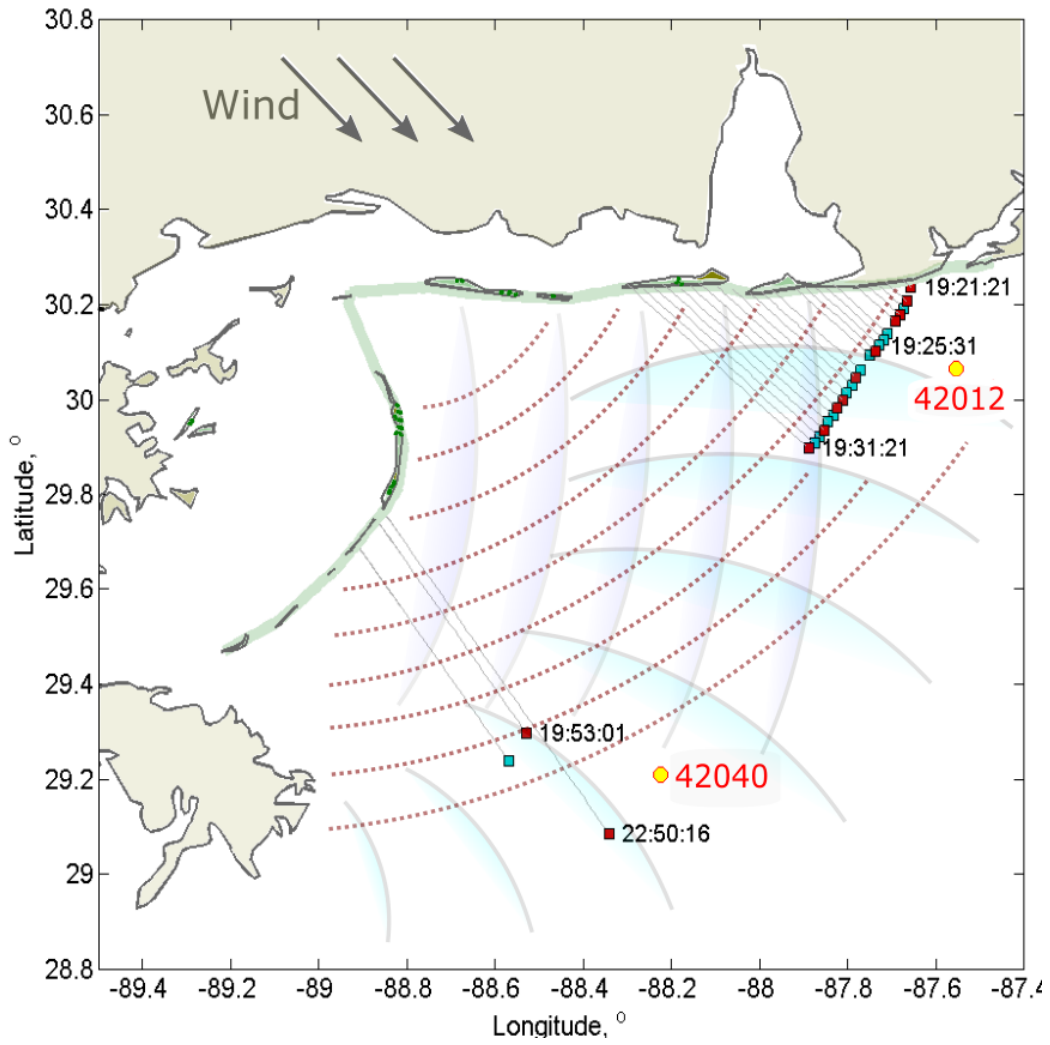


Figure 5: Locations of the images acquired on 23-Jan-2016 near NDBC buoys 42012 and 42040, and schematic wave systems orientations.

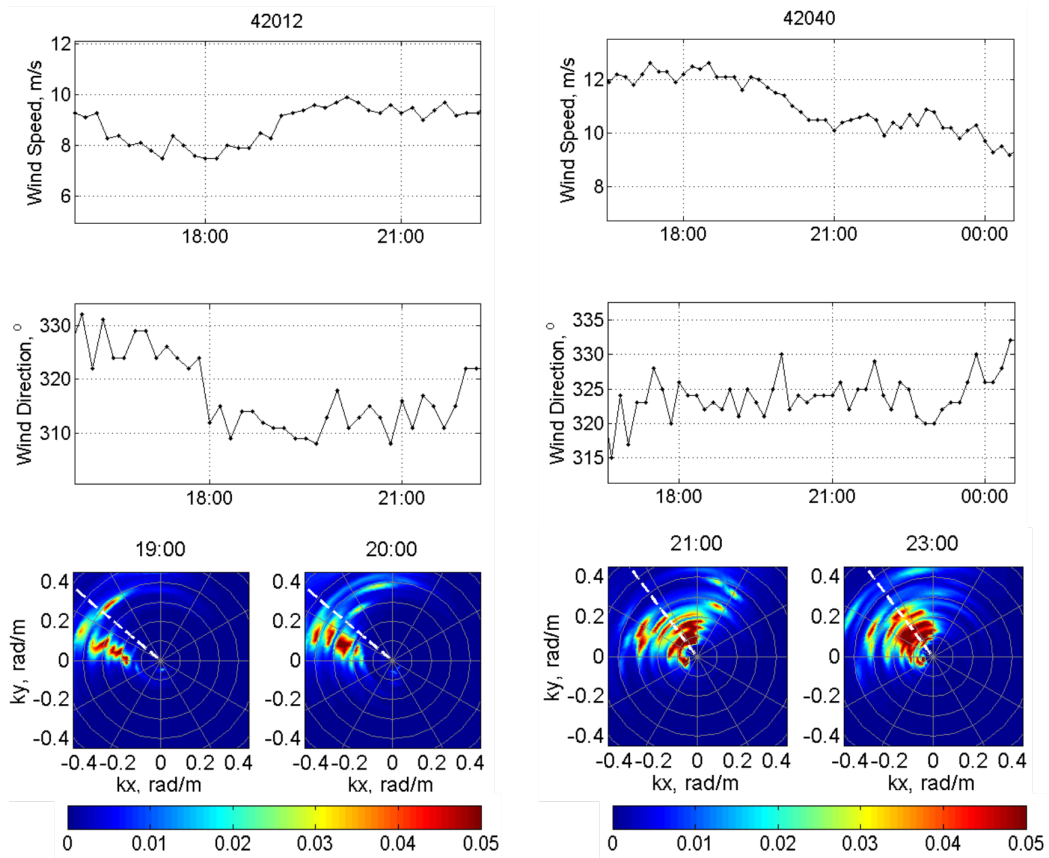


Figure 6: Windspeed, wind direction and directional slope spectra from NDBC 42012 and 42040 buoys around the time of airplane flight. Wind and wave directions are ‘from’ in nautical system.

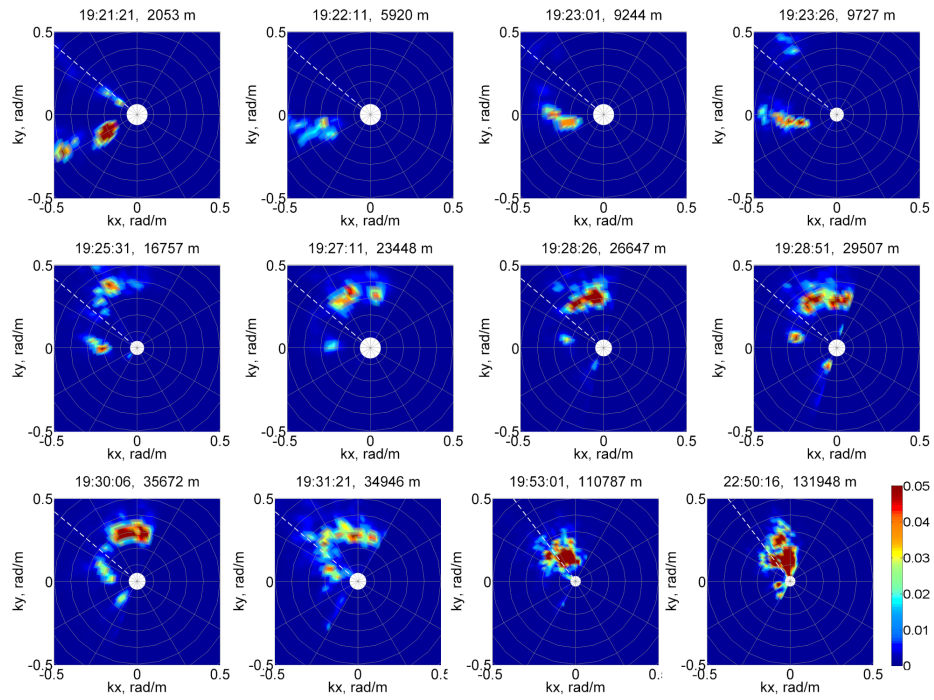


Figure 7: Directional slope spectra at the points marked by red squares on fig 5. White line is the wind direction from buoy data (trigonometrical system). Spectrum develops in presence of swell from West. Wind wave peak grows and shifts towards low wavenumbers, slightly deviates from NDBC wind direction (actually the wind also changed its direction).

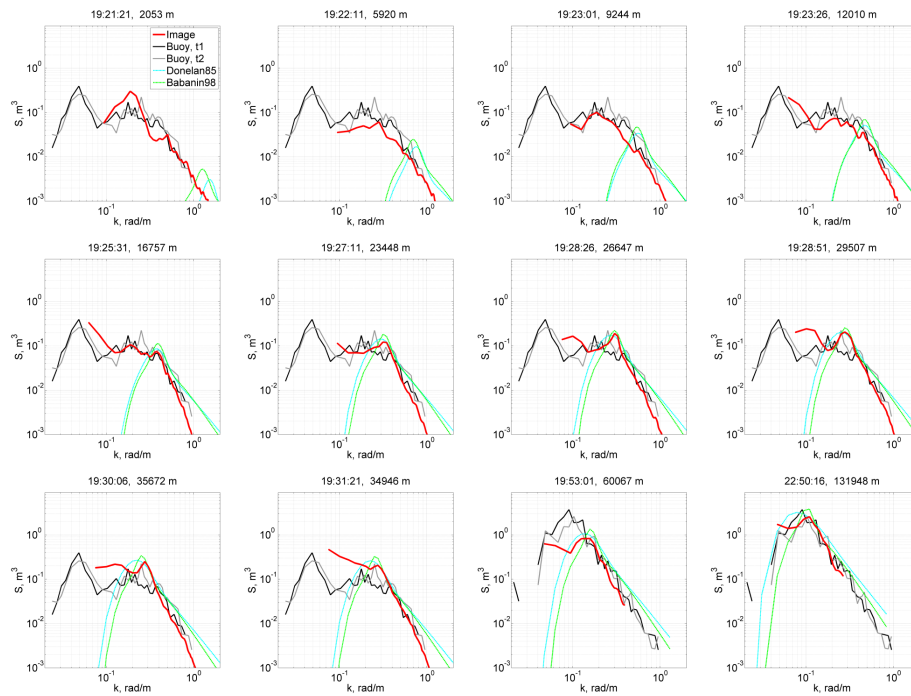


Figure 8: Omnidirectional spectra at the points marked by red squares on fig 5. Wind peak grows and shifts towards lower wavenumbers in consistence with Donelan et al. (1985) and Babanin and Soloviev (1998) spectra. Blue (Babanin and Soloviev, 1998) and green (Donelan et al., 1985) curves are given for the wind speed taken from the nearest buoy (42012 or 42040) and the fetch is corrected accounting for the spectrum wind wave peak direction estimated from Fig. 7.

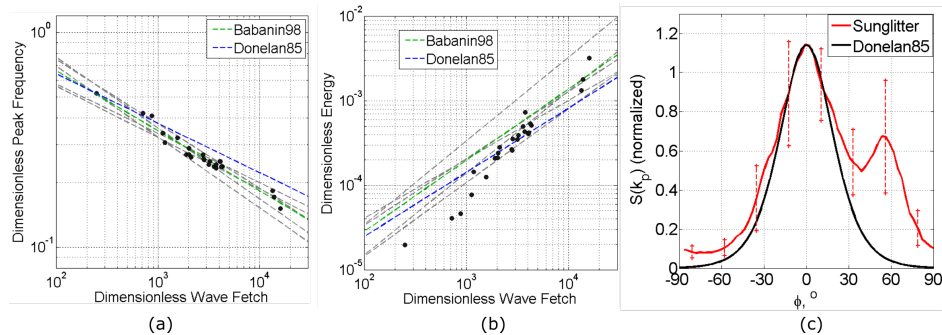


Figure 9: (a) Dimensionless peak frequency vs. dimensionless fetch. Black circles – experimental points (all retrieved spectra), dashed lines – approximations from other authors (Davidan, 1980; Babanin and Soloviev, 1998; Donelan et al., 1985; Kahma, 1981; Dobson et al., 1989; Wen et al., 1989; Ewans and C. Kibblewhite, 1990) for the wind speed 9 m s⁻¹; (b) Dimensionless peak frequency vs. windsea dimensionless variance with the same notations; (c) angular function suggested by Donelan et al. (1985) and ensemble average wave energy distribution around the peak wavenumber ($0.75k_p < k < 1.25k_p$); the length of vertical lines is equal to standard deviation.

339 6. Method Applicability and Constraints

340 As demonstrated, the proposed spectral reconstruction robustly applies
 341 when several requirements are satisfied.

342 The photograph should contain a part of sunglitter ellipse, $Z_n^2 = s^2$,
 343 within the camera incidence angle range $\theta < 50^\circ$. The area must be large
 344 enough to provide sufficient angle diversity between the transfer function vec-
 345 tors that are about normal to the ellipse. This ensures to properly eliminate
 346 the singularity of the transfer function. The brightness of the observed area
 347 should not be saturated. A saturation shortens the range of slope values.
 348 Clouds are also to be avoided. Cloudiness, or other inhomogeneities, impact

349 the estimation of the mean brightness characteristics.

350 The question of the impact of wave breaking is still open. Breakers
351 can appear on the image as bright spots, to possibly distort the retrieved
352 slope/elevation distribution. Under high-wind conditions, individual break-
353 ers shall be excluded, and individual breaking crests possibly interpolated.

354 Coming back to the part of the sunlint where the spectrum can be de-
355 rived, i.e. $0.5 < Z_n^2/s^2 < 2$ and $\theta < 50^\circ$, a simplified one-dimensional analysis
356 leads to a necessary condition for the camera zenith angle: $\beta_1 < |\theta - \theta_s| < \beta_2$,
357 where $\beta_1 = 2 \arctan \sqrt{0.5s^2}$, $\beta_2 = 2 \arctan \sqrt{2s^2}$ with $s^2 = 0.003 + 0.00512U_{10}$
358 (Cox and Munk, 1956). Close to the camera nadir direction (Fig. 1), the
359 distance between the two curves represents the longest wavelength being de-
360 tected,

$$d_{long} = H [\tan(\theta_s - \beta_1) - \tan(\theta_s - \beta_2)], \quad (7)$$

361 where H is the plane altitude.

362 The shortest wavelength being detected depends on the camera technical
363 parameters, the camera view angle, γ , and the image pixel size, N_p . The 1D
364 spatial resolution, the Nyquist wavelength, in and around the vicinity of the

365 lens optical line-of sight axis, reads:

$$d_{short} = \frac{4H \tan(\gamma/2)}{N_p \cos \theta}, \quad (8)$$

366 for an altitude H and zenith angle θ .

367 Values of d_{long} for different sun zenith angles and different wind speeds,
368 and of d_{short} for $N_p = 1000$, different camera view angles and two boundary
369 camera zenith angles θ (nadir and 50°), are presented in Fig 10, a, b, as
370 functions of camera altitude. It summarizes the range of wave scales that
371 can potentially be resolved from a sunglitter photograph.

372 As shown, Fig. 3, f, and Fig 8, measurements from an altitude $H \simeq$
373 $1 - 1.5$ km, with $N_p \simeq 2000$, $\theta_s \simeq 45^\circ$, $\gamma = 80^\circ$, provide a wave spectrum
374 defined in a range between 3-5 m to 200-300 m as predicted by fig. 10, but
375 the effective reliable range is much more reduced: from 10-20 m to 50-60
376 m. At high wavenumbers, the estimate (8) is certainly too optimistic, com-
377 pared to the real optical resolution possible to achieve. Indeed, the estimate
378 stands for the case of perfect focusing lens, and total absence of any blurring
379 effects from airplane movements and/or camera jitters. In the present ex-
380 periment, these ideal conditions are not realized, leading to an effective 2-3

381 pixel smoothing of the image brightness.

382 For the lower wavenumber limit, a reliable spectrum estimation shall require
383 a window size to encompass at least three to five wavelengths of dominant
384 surface waves, especially considering the singularity of the transfer function
385 around $k = 0$. Thus, the practical maximum wavelength is at least three
386 times shorter than d_{long} .

387 In addition, as recently discussed by Yurovsky et al. (2018) to analyze radar
388 measurements, low-frequency parts of derived spectra may be corrupted by
389 a "non-linear energy leak" process, from the spectral peak towards lower fre-
390 quencies. This effect results from the non-linearity of the modulation transfer
391 function (MTF). Accordingly to their Fig. 11, an artificial amplification of
392 the spectrum in the low-frequency range, at frequencies lower than the spec-
393 tral peak frequency, is solely governed by the MTF magnitude. In terms
394 of sunglitter imagery, the MTF, which quantifies the short wave modula-
395 tions by the underlying longer waves, is equal to: $M_i = 1/B_0 \partial B / \partial Z_i \approx$
396 $-2Z_j/s^2$ (see eq. 9 of Kudryavtsev et al. (2017a)). For winds around 5-7
397 m/s, $s^2 \approx 0.04$, and observing conditions $0.5 < Z_n^2/s^2 < 2$, the MTF range
398 becomes $M = 7 - 14$. Referring to Fig.11 by Yurovsky et al. (2018), we may
399 postulate that such rather large MTF values could artificially enhance the

400 low-frequency spectral level, $\sim (0.1 - 0.3)S(k_p)$ (to the left of the spectral
401 peak), increasing up to $(0.7 - 1.0)S(k_p)$ with decreasing wavenumber. These
402 estimates agree well with reported spectral levels at low-wavenumbers, Fig. 3,
403 f, and Fig. 8. As understood, this "non-linear energy leak" process relates
404 to the impact of spectral peak modulations on the retrieved spectral levels
405 in adjacent low-frequency intervals. Correspondingly, if the spectral peak
406 wavelength is larger than d_{long} , the retrieved spectrum shall be valid over the
407 full wavenumber range, as e.g. in the cases on upper subplots of Fig. 8.
408 Thus, despite some additional constraints, nominal estimates given in Fig. 10
409 are useful to guide experiments and the analysis for different situations. With
410 growing airborne and photo/video technique capabilities, the method validity
411 range shall likely rapidly improve, mostly thanks to increased image resolu-
412 tion and measurements taken at higher altitudes.

413 As a final remark, we note that, to retrieve spatio-temporal wave char-
414 acteristics, the requirement of a perfect sunglint is less strict. Indeed, those
415 characteristics can be derived directly from the surface brightness field and
416 do not need the surface elevation spectrum. The previous stringent require-
417 ments apply to robustly retrieve the wave elevation spectrum from a sunglint
418 photograph. Other spatio-temporal wave characteristics, such as the deter-

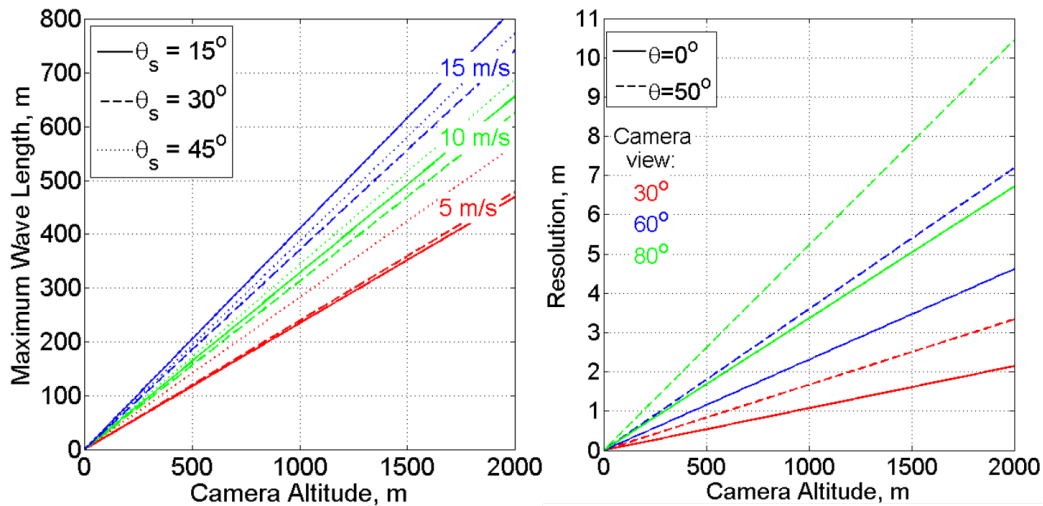


Figure 10: Left: the longest waves which can be observed within the useful part of the sunglint ($0.5 < Z_n^2/s^2 < 2$), as function of the camera altitude H . Three different sun zenith angles ($\theta_s = 15, 30, 45^\circ$) and three different wind speeds (5, 10, 15 m s^{-1}) are used for the calculations. Right: surface resolution as a function of camera altitude for the image size $N_p = 1000$ pixels, different camera view angles and two camera zenith angles ($\theta = 0^\circ$ and $\theta = 50^\circ$)

419 mination of a surface current-induced Doppler shift in the dispersion relation,
 420 merely needs to follow individual wave crests. As such, it can be applied fur-
 421 ther away from the sunglint, or even using the sky glint. Yet, a perfect
 422 geolocation might be required to accurately estimate wavelengths and shifts,
 423 and it is therefore recommended to work with images at small incidence
 424 angles.

425 7. Conclusion

426 In this paper, the efficient implementation of a two-dimensional wave
427 spectrum reconstruction algorithm has been demonstrated and applied to
428 analyze airborne sunglitter photographs acquired during an experiment in
429 the Gulf of Mexico. A linear transfer function to relate the image brightness
430 variations to surface elevations is simply deduced from the shape of the glint.
431 The singularity in wavenumber space, inherent to this approach, is eliminated
432 by using several image fragments corresponding to different directions of the
433 transfer function gradient. This was earlier suggested by Bolshakov et al.
434 (1988) and Lupyan (1988), and was also applied to drone measurements
435 (Yurovskaya et al., 2018) and satellite observations by Kudryavtsev et al.
436 (2017a). Following this methodology, the absolute wavenumber elevation
437 spectrum does not require any additional assumption or ancillary information
438 about the sky brightness, wind or wave energy.

439 As also demonstrated, a cross-correlation analysis between consecutive
440 photographs, taken with a small time lag (0.5 s), resolves the 180-degree
441 ambiguity to provide the wave direction. Further, using a transect in the
442 resulting phase spectrum gives an estimate of the wave dispersion along the
443 propagation direction. As tested, comparisons between retrieved spectra and

444 nearby NDBC buoy estimates are in good agreement, for both the spectral
445 level and energy angular distribution.

446 A case study corresponding to the wave spectral evolution with increas-
447 ing distance from shore in slanting-fetch conditions has then been considered,
448 and further provide convincing evidence of the applicability and validity of
449 the proposed method. Indeed, energy level and peak position transforma-
450 tion agree well with established approximations and laws of the wind-sea
451 development, and quantitatively compare with previous experimental data
452 and model predictions (Donelan et al., 1985; Babanin and Soloviev, 1998;
453 Ardhuin et al., 2007).

454 In the context of today’s rapidly growing technologies and the devel-
455 opment of relatively simple remote controlled measurements from drones,
456 the straightforward algorithm described here will provide efficient means to
457 renew and enhance the interest of aerial photographs of ocean sunglint pat-
458 terns. Combined with the satellite sunglitter data processing (Kudryavt-
459 sev et al., 2017a), such measurements could provide wave characteristics at
460 shorter scales, to infer comprehensive quantitative information about surface
461 wave properties and related rapid transformations over coastal areas.

462 **Acknowledgment**

463 We are grateful to Fabrice Ardhuin for the help in NDBC data process-
 464 ing and to Vladimir Dulov for the fruitful discussions. The work was sup-
 465 ported by Russian Science Foundation via grant 17-77-30019. The support
 466 of FASO of Russia under the State Assignment (No. 0827-2018-0003) and
 467 ESA SARONG project are also acknowledged.

468 **Appendix A. Symbol Definitions**

Symbol	Definition
β	Tilt angle for sunlight specular reflection
γ	Camera view angle
ζ_1, ζ_2	Surface slope components
θ	Camera zenith angle
θ_s	Sun zenith angle
ξ	Surface elevation
ρ	Fresnel reflection coefficient
Φ	Wave phase spectrum
ϕ	Wave vector angle
ϕ_ν	Camera azimuth angle
ϕ_s	Sun azimuth angle

469

B	Modified image brightness, $\sim N \cos \theta / \rho$
B_0	Mean (smoothed) image brightness
c	Wave phase velocity
E	Wave peak energy
Es	Solar radiance
f_p	Spectrum peak frequency
G_i	Brightness gradient components, $\partial B / \partial x_i$
G_{zi}	Transfer function components, $\partial B / \partial Z_i$
g	Earth gravity, 9.8 ms^{-1}
H	Camera altitude
I_i	Image brightness fragments
k	Wavenumber vector
k_p	Spectrum peak wavenumber
L	Wave fetch
M	Modulation transfer function
N	Reflected radiance
N_p	Image pixel size
N_{back}	Background radiance (sky reflected and scattered)
P	Probability density of slope components
S_ξ	Surface elevation spectrum
S_B	Surface brightness spectrum
s^2	Surface mean square slope (MSS)
U_{10}	Wind speed at 10 m
Z_1, Z_2	Surface slope components, providing specular reflection
Z_n	Specular slope absolute value, $\sqrt{Z_1^2 + Z_2^2}$

- 471 Apel, J. R., Byrne, H. M., Proni, J. R., Charnell, R. L., 1975. Observations
472 of oceanic internal and surface waves from the earth resources technology
473 satellite. *Journal of Geophysical Research* 80 (6), 865–881.
474 URL <http://dx.doi.org/10.1029/JC080i006p00865>
- 475 Ardhuin, F., Herbers, T. H. C., Watts, K. P., van Vledder, G. P., Jensen, R.,
476 Graber, H. C., 2007. Swell and slanting-fetch effects on wind wave growth.
477 *Journal of Physical Oceanography* 37 (4), 908–931.
478 URL <https://doi.org/10.1175/JP03039.1>
- 479 Babanin, A., Soloviev, Y., 1998. Field Investigation of Transformation of the
480 Wind Wave Frequency Spectrum with Fetch and the Stage of Development.
481 *Journal of Physical Oceanography* 28 (4), 563–576.
- 482 Barber, N. F., 1949. A Diffraction Analysis of a Photograph of the Sea.
483 *Nature* 164 (485).
- 484 Barber, N. F., Dec. 1954. Finding the Direction of Travel of Sea Waves.
485 *Nature* 174, 1048–1050.
- 486 Barrick, D. E., Lipa, B. J., 1985. Mapping surface currents. *Sea Technology*,
487 42.
- 488 Bolshakov, A. N., Burdyugov, V. M., Grodsky, S. A., Kudryavtsev, V. N.,
489 1988. The spectrum of energy containing surface waves as derived from
490 sun glitter images. *Issledovaniye Zemli iz Kosmosa* 5, 11–18.
- 491 Breon, F. M., Henriot, N., 2006. Spaceborne observations of ocean glint re-
492 flectance and modeling of wave slope distributions. *Journal of Geophysical*

493 Research: Oceans 111 (C6), n/a–n/a, c06005.
494 URL <http://dx.doi.org/10.1029/2005JC003343>

495 Caudal, G., Hauser, D., Valentin, R., Gac, C. L., 2014. Kuros: A new air-
496 borne ku-band doppler radar for observation of surfaces. *Journal of Atmo-*
497 *spheric and Oceanic Technology* 31 (10), 2223–2245.
498 URL <https://doi.org/10.1175/JTECH-D-14-00013.1>

499 Cox, C., Munk, W., 1954. Measurement of the roughness of the sea surface
500 from photographs of the sun’s glitter. *Journal of the Optical Society of*
501 *America* (1917-1983) 44, 838.

502 Cox, C., Munk, W., 1956. Slopes of the sea surface deduced from photographs
503 of sun glitter. *Bulletin of the Scripps Institution of Oceanography* 6 (9),
504 401–488.

505 D’Asaro, E. A., Shcherbina, A. Y., Klymak, J. M., Molemaker, J., Novelli,
506 G., Guigand, C. M., Haza, A. C., Haus, B. K., Ryan, E. H., Jacobs, G. A.,
507 Huntley, H. S., Laxague, N. J. M., Chen, S., Judt, F., McWilliams, J. C.,
508 Barkan, R., Kirwan, A. D., Poje, A. C., Özgökmen, T. M., 2018. Ocean
509 convergence and the dispersion of flotsam. *Proceedings of the National*
510 *Academy of Sciences*.
511 URL <http://www.pnas.org/content/early/2018/01/09/1718453115>

512 Davidan, I. N., 1980. Investigation of wave probability structure on field data.
513 *GOIN 151* 151, 8–26.

514 De Michele, M., Leprince, S., Thiebot, J., Raucoules, D., Binet, R., 07 2012.
515 Measurement of ocean waves velocity fields from a single spot-5 dataset

516 using correlation between panchromatic and multispectral bands. Remote
517 Sensing of Environment 199, 266–271.

518 Dobson, F., Perrie?, W., Toulany, B., 03 1989. On the deep-water fetch laws
519 for wind?generated surface gravity waves. Atmosphere-Ocean 27, 210–236.

520 Donelan, M., Hamilton, J., Hui, W., 1985. Directional spectra of wind-
521 generated ocean waves. Philosophical Transactions of the Royal Society of
522 London A: Mathematical, Physical and Engineering Sciences 315 (1534),
523 509–562.
524 URL <http://rsta.royalsocietypublishing.org/content/315/1534/509>

525 Dugan, J., Piotrowski, C., 02 2003. Surface current measurements using air-
526 borne visible image time series 84, 309–319.

527 Ewans, K., C. Kibblewhite, A., 09 1990. An examination of fetch-limited
528 wave growth off the west coast of new zealand by a comparison with the
529 jonswap results. Journal of Physical Oceanography - J PHYS OCEANOGR
530 20, 1278–1296.

531 Hennings, I., Matthews, J., Metzner, M., 1994. Sun glitter radiance and radar
532 cross-section modulations of the sea bed. Journal of Geophysical Research:
533 Oceans 99 (C8), 16303–16326.
534 URL <http://dx.doi.org/10.1029/93JC02777>

535 Herbers, T. H. C., Jessen, P. F., Janssen, T. T., Colbert, D. B., MacMahan,
536 J. H., 2012. Observing ocean surface waves with gps-tracked buoys. Journal
537 of Atmospheric and Oceanic Technology 29 (7), 944–959.
538 URL <https://doi.org/10.1175/JTECH-D-11-00128.1>

- 539 Kahma, K., 10 1981. A study of the growth of the wave spectrum with fetch.
540 Journal of Physical Oceanography 11, 1503–1515.
- 541 Kudryavtsev, V., Myasoedov, A., Chapron, B., Johannessen, J. A., Col-
542 lard, F., 2012. Imaging mesoscale upper ocean dynamics using synthetic
543 aperture radar and optical data. Journal of Geophysical Research: Oceans
544 117 (C4), n/a–n/a, c04029.
545 URL <http://dx.doi.org/10.1029/2011JC007492>
- 546 Kudryavtsev, V., Myasoedov, A., Chapron, B., Johannessen, J. A., Collard,
547 F., 2012. Joint sun-glitter and radar imagery of surface slicks. Remote
548 Sensing of Environment 120 (Supplement C), 123 – 132, the Sentinel
549 Missions - New Opportunities for Science.
550 URL <http://www.sciencedirect.com/science/article/pii/S0034425712000831>
- 551 Kudryavtsev, V., Yurovskaya, M., Chapron, B., Collard, F., Donlon, C.,
552 2017a. Sun glitter imagery of ocean surface waves. Part 1: Directional spec-
553 trum retrieval and validation. Journal of Geophysical Research: Oceans
554 122 (2), 1369–1383.
- 555 Kudryavtsev, V., Yurovskaya, M., Chapron, B., Collard, F., Donlon, C.,
556 2017b. Sun glitter imagery of surface waves. Part 2: Waves transformation
557 on ocean currents. Journal of Geophysical Research: Oceans 122 (2), 1384–
558 1399.
- 559 Lupyan, E. A., 1988. Retrieval of the angular energy distribution of two-
560 dimensional elevation spectrum from optical image of the sea surface. Issle-
561 dovaniye Zemli iz Kosmosa 3, 31–35.

- 562 Lygre, A., Krogstad, H. E., 1986. Maximum entropy estimation of the
563 directional distribution in ocean wave spectra. *Journal of Physical*
564 *Oceanography* 16 (12), 2052–2060.
565 URL [https://doi.org/10.1175/1520-0485\(1986\)016<2052:MEEOTD>2.0.CO;2](https://doi.org/10.1175/1520-0485(1986)016<2052:MEEOTD>2.0.CO;2)
- 566 Melville, W. K., Lenain, L., Cayan, D. R., Kahru, M., Kleissl, J. P., Linden,
567 P. F., Statom, N. M., 2016. The modular aerial sensing system. *Journal of*
568 *Atmospheric and Oceanic Technology* 33 (6), 1169–1184.
569 URL <https://doi.org/10.1175/JTECH-D-15-0067.1>
- 570 Monaldo, F. M., Kasevich, R. S., 1981. Daylight imagery of ocean surface
571 waves for wave spectra. *Journal of Physical Oceanography* 11 (2), 272–283.
572 URL [https://doi.org/10.1175/1520-0485\(1981\)011<0272:DI00SW>2.0.CO;2](https://doi.org/10.1175/1520-0485(1981)011<0272:DI00SW>2.0.CO;2)
- 573 Nieto, B., Rodrigues, G., Hessner, K., Gonzalez, B., 2004. Inversion of ma-
574 rine radar images for surface wave analysis. *Journal of Atmospheric and*
575 *Oceanic Technology* 21, 1291–1300.
- 576 Rascle, N., Molemaker, J., Mari?, L., Noguier, F., Chapron, B., Lund,
577 B., Mouche, A., 2017. Intense deformation field at oceanic front inferred
578 from directional sea surface roughness observations. *Geophysical Research*
579 *Letters* 44 (11), 5599–5608, 2017GL073473.
580 URL <http://dx.doi.org/10.1002/2017GL073473>
- 581 Rascle, N., Noguier, F., Chapron, B., Mouche, A., Ponte, A. l., 2016. Surface
582 roughness changes by finescale current gradients: Properties at multiple
583 azimuth view angles. *Journal of Physical Oceanography* 46 (12), 3681–
584 3694.

- 585 Senet, C. M., Seeman, J., Flampouris, S., Ziemer, F., 2008. Determination
586 of Bathymetric and Current Maps by the Method DiSC Based on the
587 Analysis of Nautical X-Band Radar Image Sequences of the Sea Surface.
588 IEEE Transactions on Geoscience and Remote Sensing 46 (8), 2267–2279.
- 589 Spooner, J., 1822. Sur la lumiere des ondes de la mer. *Corresp. Astronomique*
590 du Baron de Zach 6, 331.
- 591 Stilwell, D., 1969. Directional energy spectra of the sea from photographs.
592 *Journal of Geophysical Research* 74 (8), 1974–1986.
593 URL <http://dx.doi.org/10.1029/JB074i008p01974>
- 594 Stilwell, D., Pilon, R. O., 1974. Directional spectra of surface waves from
595 photographs. *Journal of Geophysical Research* 79 (9), 1277–1284.
596 URL <http://dx.doi.org/10.1029/JC079i009p01277>
- 597 Walsh, E. J., Vandemark, D. C., Friehe, C. A., Burns, S. P., Khelif, D., Swift,
598 R. N., Scott, J. F., 1998. Measuring sea surface mean square slope with a
599 36-ghz scanning radar altimeter. *Journal of Geophysical Research: Oceans*
600 103 (C6), 12587–12601.
601 URL <http://dx.doi.org/10.1029/97JC02443>
- 602 Wen, S. C., Zhang, D. C., Guo, P. Z., Chen, B. H., 1989. Parameters in
603 wind?wave frequency spectra and their bearings on spectrum forms and
604 growth. *Acta Oceanol. Sinica* 8, 15–39.
- 605 Yurovskaya, M., Kudryavtsev, V., S. Shirokov, A., Yu. Nadolya, I., 01
606 2018. Field measurements of the sea surface wave spectrum from pho-

607 tos of sunglitter taken from drone. *Sovremennye problemy distantsionnogo*
608 *zondirovaniya Zemli iz kosmosa* 15, 245–257.

609 Yurovsky, Y. Y., Kudryavtsev, V. N., Grodsky, S. A., Chapron, B., 2018.
610 Low-frequency sea surface radar doppler echo. *Remote Sensing* 10 (6).

611 **List of Figure Captions**

612 **Figure 1**

613 (a) The observation area with NDBC buoy locations (gray diamonds). Green
614 star shows location of the analysis on 11-Feb-2016 (section 4), colors are the
615 tracks of the 23-Jan-2016 flight (section 5). (b) Sketch of the field of view
616 of the afterward camera, for a flight altitude of 1000 m. Here we show the
617 special case of the sun exactly at the rear of the airplane when the specular
618 sun spot is at the center of the camera field of view. The ellipse is the
619 contour $Z_n^2 = s^2$ (see the notifications below). The white arrows show the
620 orientations of the transfer function gradient, G_{zi} .

621 **Figure 2**

622 (a) An airborne snapshot of a sea surface; (b) image projected on the sea
623 surface plane (x-label is to the East, y-label is to the North, two ellipses
624 determine the zone $0.5 < Z_n^2/s^2 < 2$); (c) pixel intensities for the left col-
625 umn of a photo (dots) and their polynomial approximation indicating the
626 background radiation; (d) $\cos \theta/\rho$ field; (e) $B = (N - N_{back}) \cos \theta/\rho$ field; (f)
627 mean brightness field, B_0

628 **Figure 3**

629 (a) Square fragments (450 m size) of brightness variation field, $(B - B_0)$, taken
630 for spectrum retrieval. Two ellipses determine the zone $0.5 < Z_n^2/s^2 < 2$,
631 black line is $\theta = 50^\circ$; (b) The sum of brightness spectra; (c) the trans-
632 fer function, $\sum_{n=1}^N (G_{zi}^m k_i)^2$; (d) retrieved from (6) elevation spectrum; (e)
633 NDBC buoy data directional spectrum (42012); (f) Omnidirectional spectra
634 comparison.

635 **Figure 4**

636 (a)-(b) Snapshots of the same location taken with 0.5 s time shift; (c) co-
637 herence of two brightness fields; (d) phase shift; wave direction (from) corre-
638 sponds to positive values of a phase shift; (e) dispersion relation calculated
639 from a phase shift along the line of coherence maximum (dashed lines in (c)
640 and (d) plots).

641 Figure 5

642 Locations of the images acquired on 23-Jan-2016 near NDBC buoys 42012
643 and 42040, and schematic wave systems orientations.

644 Figure 6

645 Windspeed, wind direction and directional slope spectra from NDBC 42012
646 and 42040 buoys around the time of airplane flight. Wind and wave directions
647 are “from” in nautical system.

648 Figure 7

649 Directional slope spectra at the points marked by red squares on fig 5. White
650 line is the wind direction from buoy data (trigonometrical system). Spectrum
651 develops in presence of swell from West. Wind wave peak grows and shifts
652 towards low wavenumbers, slightly deviates from NDBC wind direction (ac-
653 tually the wind also changed its direction).

654 Figure 8

655 Omnidirectional spectra at the points marked by red squares on fig 5. Wind
656 peak grows and shifts towards lower wavenumbers in consistence with Donelan
657 et al. (1985) and Babanin and Soloviev (1998) spectra. Blue (Babanin and
658 Soloviev, 1998) and green (Donelan et al., 1985) curves are given for the
659 wind speed taken from the nearest buoy (42012 or 42040) and the fetch is
660 corrected accounting for the spectrum wind wave peak direction estimated

661 from Fig. 7.

662 Figure 9

663 (a) Dimensionless peak frequency vs. dimensionless fetch. Black circles –
664 experimental points (all retrieved spectra), dashed lines – approximations
665 from other authors (Davidan, 1980; Babanin and Soloviev, 1998; Donelan
666 et al., 1985; Kahma, 1981; Dobson et al., 1989; Wen et al., 1989; Ewans and
667 C. Kibblewhite, 1990) for the wind speed 9 m s^{-1} ; (b) Dimensionless peak fre-
668 quency vs. windsea demensionless variance with the same notations; (c) an-
669 gular function suggested by Donelan et al. (1985) and ensemble average wave
670 energy distribution around the peak wavenumber ($0.75k_p < k < 1.25k_p$); the
671 length of vertical lines is equal to standard deviation.

672 Figure 10

673 Left: the longest waves which can be observed within the useful part of the
674 sunglint ($0.5 < Z_n^2/s^2 < 2$), as function of the camera altitude H . Three
675 different sun zenith angles ($\theta_s = 15, 30, 45^\circ$) and three different wind speeds
676 ($5, 10, 15 \text{ m s}^{-1}$) are used for the calculations. Right: surface resolution as
677 a function of camera altitude for the image size $N_p = 1000$ pixels, different
678 camera view angles and two camera zenith angles ($\theta = 0^\circ$ and $\theta = 50^\circ$)